(Received 21 September 2024, Accepted 5 November 2024, Scheduled 16 November 2024)

Design and Optimization of Series-Connected Hybrid Excitation Permanent Magnet Synchronous Motor

Jianwei Liang, Tian Song*, Peiyao Guo, Xiubin Zhu, Zhangsheng Liu, and Yuqian Zhao

Jiangxi University of Science and Technology, China

ABSTRACT: To address the problems that the traditional permanent magnet synchronous motor airgap flux is difficult to adjust and that the weak magnetic speed expansion ability is poor, a new series-connected hybrid excitation permanent magnet synchronous motor is proposed. A DC excitation winding is added to the rotor, allowing the excitation field generated by this winding to form a series connection with the magnetic field of the permanent magnets. The structure of this paper includes an overview of the novel rotor structure and principle of operation. For the complex rotor structure, a multi-objective genetic algorithm is used for optimization, followed by finite element analysis to compare the performance of the initial motor, the optimized motor, and the conventional motor in terms of no-load air-gap magnetism, reverse electromotive force, as well as output torque and efficiency. The magnetic load of the motor in the demagnetized state is increased from 0.2 to 0.266 compared to the unexcited state, and the magnetization capacity is improved by 33%. The output torque of the optimized motor is 252 N·m at low speed; the output torque of the conventional motor is 220 N·m; and the starting torque of the motor was improved by 14.5%. The maximum speed is increased from 10,000 rpm to 11,500 rpm, and the speed expansion capacity is enhanced by 15%. The effectiveness and feasibility of the series-connected hybrid excitation permanent magnet synchronous motor are verified.

1. INTRODUCTION

Rare-earth NdFeB material as the excitation source of Permanent Magnet Synchronous Motor (PMSM) has high remanent magnetization and high coercivity compared with traditional materials such as ferrite. This performance significantly increases automotive permanent magnet synchronous motors' power density and torque density. It has become the main material for most of the current automotive drives [1–4]. On-vehicle PMSM operates under complex conditions [5] and requires a wide speed regulation range and high efficiency range [6–9]. However, PMSM operating at low speeds results in low output power. At high speeds [10], a large d-axis inductance has to be allocated for weak magnetization, and the increase in copper consumption leads to a significant decrease in motor efficiency [11, 12], limiting the motor's ability to expand speeds.

In recent years, scholars have proposed many topologies for the problems of high-speed weak magnetism difficulty of vehicle-mounted PMSM and low efficiency of low-speed motors [13, 14]. Ref. [15] proposes a multilayer flux barrier reverse-convex pole permanent magnet synchronous motor. A circular flux barrier is created at the outer q-axis of the rotor to reduce the inductance of the q-axis for a wider constant power regulation range. Ref. [16] proposes a magnetic moment dual-tuned shaft-radial hybrid excitation motor. According to the axial-radial magnetic circuit coupling relationship and multi-field torque formation mechanism, the motor's main air gap magnetic field can be adjusted with torque enhancement. Ref. [17] adopts an improved Sinusoidal Pulse Width Modulation (SPWM) decoupling modulation strategy based on the controllability of harmonic injection. According to the requirement of wide motor speed regulation, smooth switching between modulation strategies is realized to achieve the purpose of widening the motor speed range. Refs. [18, 19] propose a speed-regulated motor in which the rotor yoke can be moved. The centrifugal force that increases when the motor speed increases causes the distance between the tile-shaped rotor yoke and permanent magnets to change and regulates the main magnetic flux of the motor. Ref. [20] presents a permanent magnet-assisted excitation motor. A small amount of permanent magnet is added inside the convex pole magnetic shoe on the basis of the induction motor, and the high-speed maximum speed of the motor is improved after optimization. Ref. [21] proposes to leave a leakage branch where the permanent magnet leakage flux and q-axis flux meet and use the alternating armature current to regulate the saturation of the leakage bridge of the motor. This realizes the effective regulation of the motor leakage flux and air gap flux, and expands the speed regulation range of the motor.

In order to achieve the extensive speed regulation capabilities of the permanent magnet synchronous motor, a hybrid exciter permanent magnet synchronous motor has been designed. This series motor has a rated power of 50 kW and a rated speed of 3000 rpm. Two excitation methods are utilized, DC excitation and permanent magnet excitation. The magnetic flux of the motor is changed by energizing the excitation winding with currents of different directions, and the magnitude of the excitation current is changed to adjust the motor dq-axis inductance accordingly. Firstly, the distribution of the no-load magnetic field of the motor is analyzed when the rotor excitation wind-

* Corresponding author: Tian Song (2568706873@qq.com).

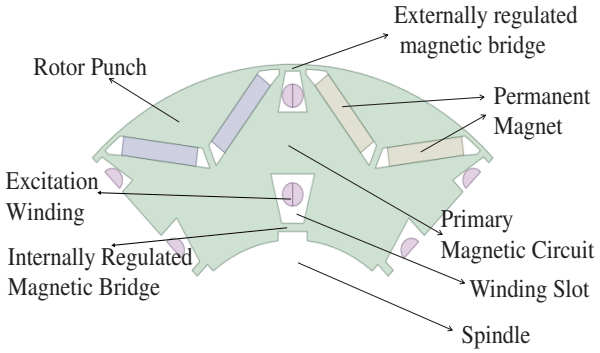

FIGURE 1. Schematic of rotor structure for series hybrid excitation.

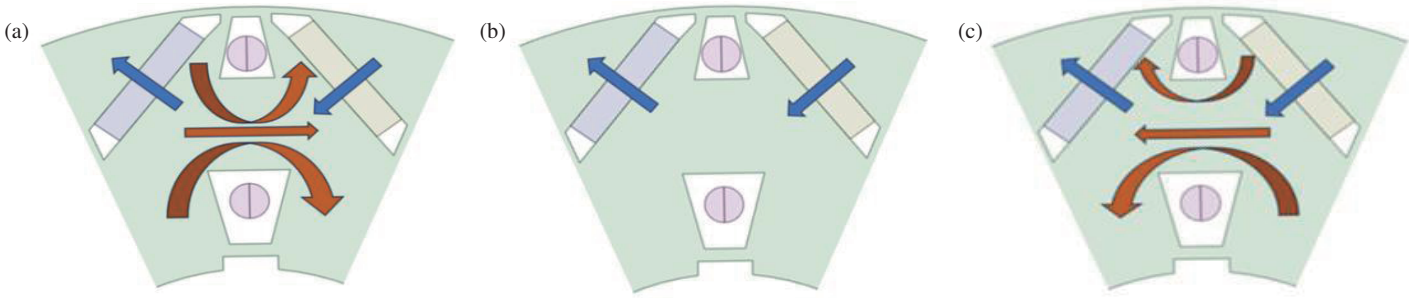

FIGURE 2. Motor magnetic potential distribution. (a) Demagnetization. (b) Non-excited. (c) Magnetization.

ing current is in the three states of magnetizing, demagnetizing, and non-excitation. The mathematical relationship between rotational speed and excitation current is derived for the motor under the conditions of high speed and weak magnetic expansion, as well as low speed and increasing torque, respectively. It provides a theoretical basis for the performance improvement of the motor. Secondly, due to the complex rotor structure of the motor, the optimized parameters are layered using sensitivity coefficients. The strong sensitive layer parameters are optimized with genetic algorithm multi-objective optimization to get the optimized parameters. Finally, the model of a conventional permanent magnet synchronous motor with the same power is introduced. The speed discretization is employed for the calculation and comparison of the two types of motors in the low-speed, high-torque condition below the rated speed, and high-speed expansion condition above the rated speed. The validity of the analysis is verified.

2. MOTOR TOPOLOGY AND PRINCIPLE

2.1. Motor Rotor Topology

In this paper, the series-connected hybrid excitation rotor structure is proposed, in which the no-load magnetic field of the motor consists of two parts: the permanent magnetic chain provided by a pair of V-type permanent magnets and the excitation chain provided by the excitation windings. The excitation winding is distributed along the radial direction in the motor q-axis, and the motor q-axis position consists of seven parts: rotor shaft, magnetic barrier, inner and outer magnetic field regulating magnetic bridges, 2 excitation winding slots, and main magnetic circuit of the motor. In contrast with the excitation winding of a conventional hybrid excitation motor, the motor rotor in this paper incorporates two internal and external regulating magnetic bridges, thus providing two supplementary closed paths for the motor magnetic circuit. The motor structure is shown in Fig. 1.

2.2. Principle of Rotor Magnetization

To facilitate the elaboration of the magnetization principle of the rotor structure, the motor operating state is divided into excitation winding demagnetization, no excitation winding, and excitation winding magnetization. The current generates the peripheral magnetic field shown in Eq. (1):

$$B = \frac{\mu N I}{2\pi r} \tag{1}$$

where B is the strength of the magnetic field around the wire, μ the permeability of the medium around the energized wire, r the radius of the magnetic lines of force, I the magnitude of the current in the wire, and N the number of turns of the wire. According to the positive and negative excitation winding currents, two magnetic field states, clockwise and counterclockwise, are excited around it. When the motor is unloaded, the three kinds of excitation windings are distributed in three states of the motor, and the distribution of their magnetic potentials is shown in Fig. 2. In order to verify the effectiveness of the topology on the magnetic field regulation, -20 A, 0 A, and 20 A currents are applied to the excitation windings, respectively, and Fig. 3 shows the magnetomotive force distribution of the motor under different excitation currents.

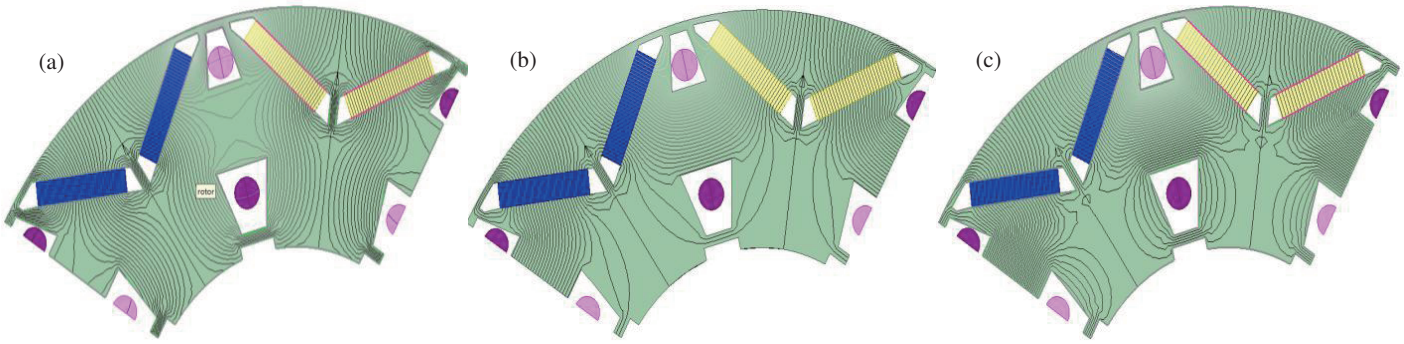

FIGURE 3. Motor magnet wire distribution. (a) $I_0 = -20$ A, (b) $I_0 = 0$ A, (c) $I_0 = 20$ A.

As can be seen from Fig. 2 and Fig. 3, when the motor excitation winding is demagnetized, the magnetic kinetic potential of the permanent magnet and the magnetic kinetic potential generated by the excitation winding are in the opposite directions, and the magnetic lines of force passing through the main magnetic circuit of the rotor are greatly reduced. When the motor is without an excitation winding state, most of the permanent magnet magnetic force lines are through the main magnetic circuit, and only a small number of magnetic force lines by the internal and external regulating magnetic bridge form a circuit. When the motor excitation winding is in the state of increasing magnetization, the magnetic kinetic potential of the permanent magnet and the magnetic kinetic potential generated by the excitation winding are in the same direction. The magnetic lines of force passing through the main magnetic circuit of the rotor increase, and saturation of the main magnetic circuit occurs. The results show that the finite element simulation results are in good agreement with the results of the magnetomotive force analysis. It is verified that the magnetic field regulation capability of the series hybrid excitation structure is proposed in this paper.

2.3. Effect of Excitation Current on Weak Magnetic Speed Expansion

The full-frequency operational range of the onboard motor can be delineated into two distinct intervals: the constant torque interval and the weak magnetic interval. The weak magnetic interval is further subdivided into two phases, designated as weak magnetic interval I and weak magnetic interval II, as illustrated in Fig. 4.

Conventional permanent magnet motors need to adjust the ratio of i_d and i_q currents when they are weakly magnetized. The component of the i_d current is increased to counteract the excessive growth of the counter electromotive force. If the reluctance torque of the motor is ignored, the electromagnetic torque is independent of i_d, and the d-axis current produces only copper consumption, resulting in a decrease in the motor output power. In contrast, the motor model proposed in this paper increases the motor speed in the ideal stat. The growth of the counter electromotive force relies on the excitation current input to the demagnetization current. To compare the motor model presented in this paper with the conventional motor in terms of speed expansion control, Fig. 5 and Fig. 6 show the voltage vector diagrams of the conventional motor and the motor in this paper at different speeds.

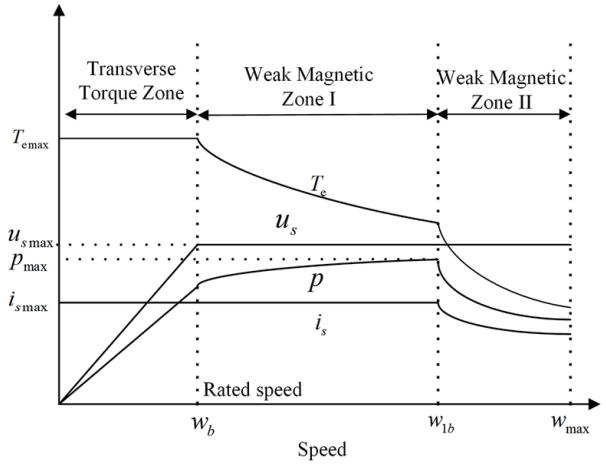

FIGURE 4. PMSM operation scope division.

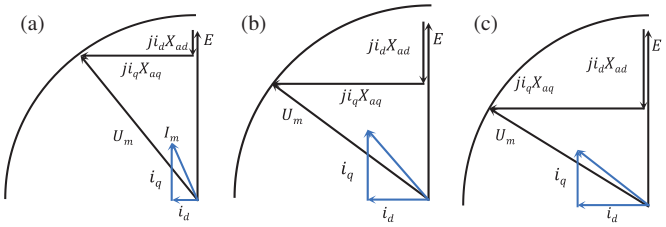

FIGURE 5. Conventional motor voltage vector diagram. (a) Constant torque region. (b) Weak magnetic region I. (c) Weak magnetic region II.

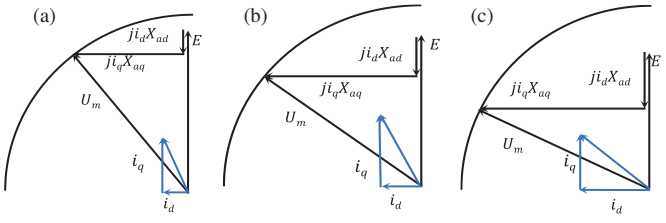

FIGURE 6. Vector diagram of motor voltage in this paper. (a) Constant torque region. (b) Weak magnetic region I. (c) Weak magnetic region II.

Maintaining the reverse electromotive force constant, the specific relationship between the excitation current and rotational speed is shown in Eq. (2):

$$\begin{aligned} E &= 4.44fNB_{av}K_{dp}\frac{D\pi}{2p}L \\ &= 4.44\frac{np}{60}N(0.00881*I+0.60936)K_{dp}\frac{D\pi}{2p}L \\ &= 4.44\frac{np}{60}N(0.60936+0.00881\,|I|)K_{dp}\frac{D\pi}{2p}L \end{aligned} \quad (2)$$

Simplifying the above equation, the direct relationship between the no-load reverse electromotive force and the demagnetizing current of the motor is shown in Equation (3):

$$\begin{aligned} |I| &= \frac{\left(0.60936-\frac{E}{n\frac{4.44p}{60}NK_{dp}\frac{D\pi}{2p}L}\right)}{0.00881} \\ &= C_1-\frac{C_2}{nC_3} \end{aligned} \quad (3)$$

where C_1, C_2, C_3 are the constant values simplified by the fixed physical parameters in Eq. (3). As can be observed from the aforementioned equation, should it be necessary to maintain the motor reverse electromotive force constant, a positive correlation can be identified between the motor demagnetizing current and rotational speed. Therefore, when the motor speed increases, the distribution ratio of the motor armature current in the d-axis is reduced by increasing the demagnetizing current. When the motor speed continues to increase, the motor armature d-axis current and rotor demagnetizing current work together to produce stronger demagnetizing electromagnetism, which achieves an increase in motor speed. The motor speed interval is shown schematically in Fig. 7.

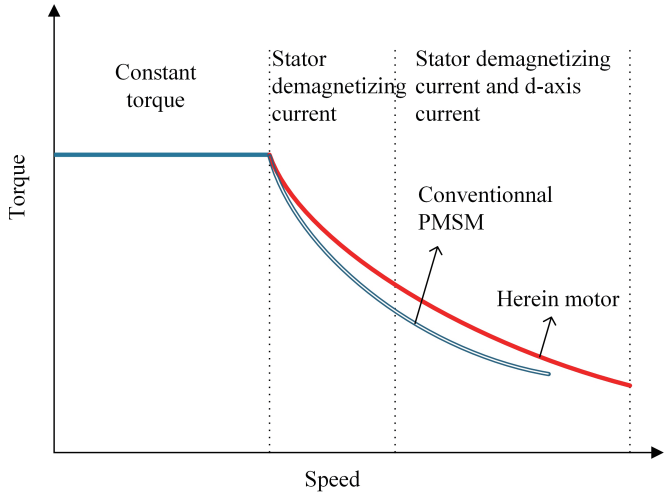

FIGURE 7. Motor speed expansion operation range division.

2.4. Effect of Excitation Current on LowSpeed Large Torque

When the motor operates at its base speed, the lower speed results in a reduction in power output. This is because at this point in time, the motor's counter electromotive force has not yet reached its peak value. In order to improve the motor's counter electromotive force and subsequently increase the motor's torque output, the rotor excitation winding is energized with magnetizing current at the lower speed of the motor. The mathematical model is shown in Equations (4) and (5):

$$\begin{aligned} E &= 4.44fNB_{av}K_{dp}\frac{D\pi}{2p}L \\ &= 4.44\frac{np}{60}N(-1.35*10^{-4}*I^2+0.008*I+0.61)K_{dp}\frac{D\pi}{2p}L \end{aligned} \quad (4)$$

$$T=\frac{9.55*p}{n}=\frac{9.55*3*E*I\cos(\alpha)\eta}{n} \quad (5)$$

The specific method is as follows:

(1) The initial step is to set the motor magnetizing current to its maximum value. Subsequently, the value of the motor speed at the point where the motor reaches the maximum terminal voltage limit must be calculated. Additionally, the value of the maximum output torque of the motor must be determined.

(2) Subsequently, the speed of the motor is increased in accordance with the synthesized voltage, which represents the maximum value of the terminal voltage. Concurrently, the magnetizing current of the rotor is diminished, and the value of the torque output at the elevated motor speed is calculated.

(3) When the motor speed reaches the rated speed, the motor rotor magnetizing current is zero, and the motor rotor excitation winding enters the current-free state.

The output performance of the motor at low speed is depicted in Fig. 8 based on the above steps. From the figure it can be seen that the motor's output torque can be increased in the magnetizing state of the motor, which overall enhances the output performance of the motor at low speeds.

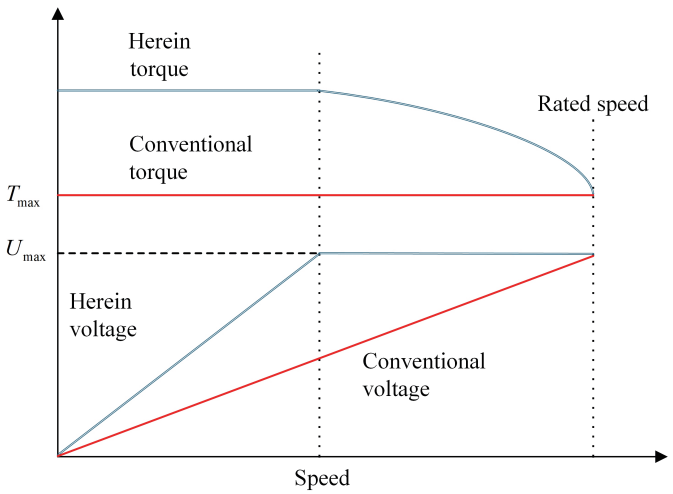

FIGURE 8. Motor low-speed operation range division.

3. DESIGN OPTIMIZATION

The initial magnetic bridge design verifies that the excitation current has the ability to regulate the air-gap magnetic field, thus improving the motor's high-speed speed expansion and low-speed large torque capability. In light of the intricate configuration of the motor rotor dimensions, a multitude of dimensions are involved in the magnetizing bridge. When a discrepancy arises between the structural parameters of this motor, it will inevitably have a direct and pronounced impact on the performance of the motor. Consequently, in this paper, the design parameters are subjected to a sensitivity analysis, which encompasses both the design parameters and target parameters. Subsequently, a multi-objective optimization genetic algorithm is proposed as a means of achieving the optimal design of the motor structure.

3.1. Machine Optimization Process

In this paper, a multi-objective genetic algorithm is used, and the specific flowchart of the motor design is shown in Fig. 9.

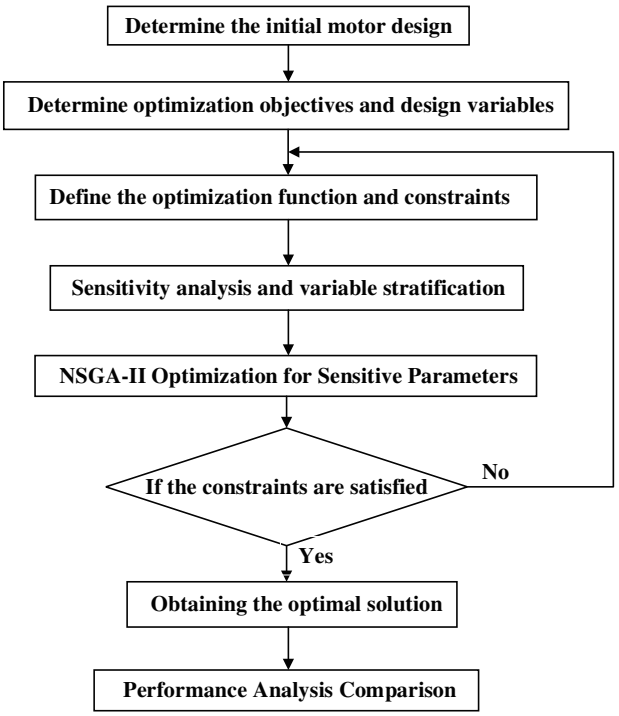

FIGURE 9. Motor design flow chart.

3.2. Optimization Objectives and Structural Optimization Parameters

In this paper, 10 structural variables that have a large impact on the performance of the motor are selected as shown in Fig. 10. The definition of each structural parameter of the rotor and its range of variation are shown in Table 1.

The vehicle-mounted, built-in, permanent magnet synchronous motor exhibits a high torque density. The low-speed high-torque performance and high-speed weak magnetic speed expansion capability of the motor are contingent upon the alteration of the air-gap magnetization density when the motor is in operation in either a demagnetized or magnetized enhanced state. The amount of change in its magnetic load compared to the unexcited state reflects the strength of the motor's magnetizing ability. The ratio of the air gap magnetic load of the demagnetized and magnetized motor to the unexcited magnetic load of the motor, δ_1 and δ_2, is taken as the optimization objective.

TABLE 1. Structural parameters and range of variation.

Structural Parameters	Variation Ranges
$alpha$	[100 deg, 125 deg]
l_{pm}	[16 mm, 23 mm]
w_o	[0.5 mm, 2 mm]
w_i	[1 mm, 3 mm]
w_{co}	[6 mm, 10 mm]
w_{ci}	[10 mm, 14 mm]
l_{ou}	[1 mm, 6 mm]
l_{od}	[6 mm, 14 mm]
l_{iu}	[8 mm, 16 mm]
l_{id}	[4 mm, 10 mm]

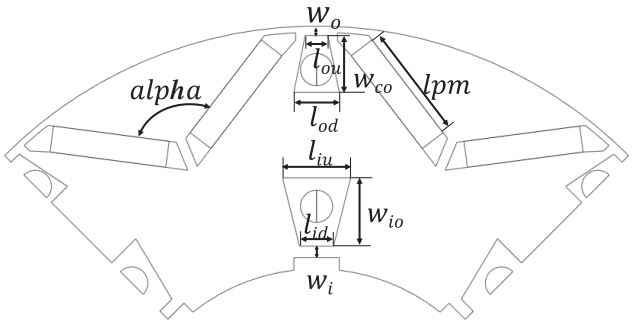

FIGURE 10. Schematic diagram of rotor parameters.

The 11th and 13th harmonics of the air gap magnetization are the main harmonics that generate 12 torque pulsations in the motor. Weakening the 11th and 13th harmonics amplitude ratio of the air gap magnetization can reduce the torque pulsations of the motor. Therefore, the 11th and 13th harmonics of air-gap magnetism amplitude percentage B_d under the unexcited magnetism of the motor are taken as the optimization objective.

Enhancing the motor's magnetizing performance should be accompanied by enhancing the motor's ability to output torque and increasing the motor's torque density parameter.

The relevant optimization objective is shown in Equations (6) to (8):

$$\delta_d = \frac{B_{0avg} - B_{davg}}{B_{0avg}} \tag{6}$$

$$\delta_u = \frac{B_{uavg} - B_{0avg}}{B_{0avg}} \tag{7}$$

$$B_d = \frac{B_{d11} + B_{d13}}{B_{d1}} \tag{8}$$

$$T = \frac{3}{2} p(\varphi_f i_q + (L_d - L_d)) i_d i_q \tag{9}$$

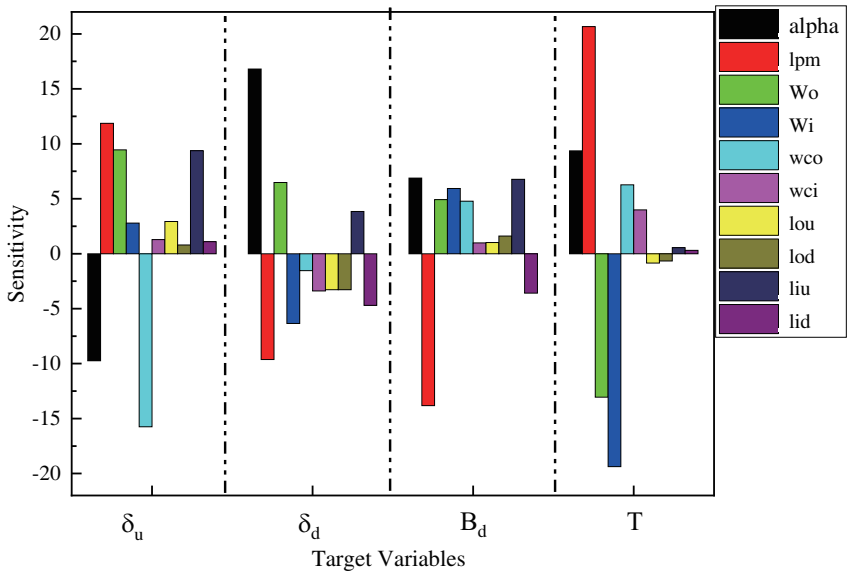

FIGURE 11. Distribution of variable sensitivities.

where B_{davg}, B_{0avg}, B_{uavg} are the magnetic loads of the air gap in demagnetization, non-excitation, and magnetization states, respectively; B_{d1}, B_{d11}, B_{d13} are the fundamental amplitude, 11th harmonic amplitude, and 13th harmonic amplitude of the air gap field density in demagnetization; B_{u1}, B_{u11}, B_{u13} are the fundamental amplitude, 11th harmonic amplitude, and 13th harmonic amplitude of the air gap field density in magnetization state.

The motor design optimization objective constraints and objective functions are shown in Eqs. (10) and (11):

$$\begin{cases} \delta_u \geq 0.15 \\ \delta_d \geq 0.25 \\ B_d \leq 0.1 \\ T \geq 120Nm \end{cases} \tag{10}$$

$$\begin{cases} f(x_i) = \lambda_{\delta d}\frac{\delta_d(x_i)}{\delta'_d} + \lambda_{\delta u}\frac{\delta_u(x_i)}{\delta'_u} + \lambda_{Bd}\frac{B_d(x_i)}{B'_d} + \lambda_T\frac{T(x_i)}{T} \\ \lambda_{\delta d} + \lambda_{\delta u} + \lambda_{Bd} + \lambda_T = 1 \\ \min x_i \leq x_i \leq \max x_i \end{cases} \tag{11}$$

where δ'_d, δ'_u, B'_d, and T' are the critical values of each optimization objective, and x_i is the design parameter that the optimization iteration is selected. The numerator value in Eq. (11) denotes the optimization iteration, which is the value of the output objective result computed from the selected design parameters. $\lambda_{\delta d}$, $\lambda_{\delta u}$, λ_{Bd}, and λ_T are the assignment factors for the proportional weights of the different optimization objectives, respectively, whose values sum up to one.

3.3. Correlation Analysis

In genetic optimization algorithm calculations, the resources used by the computer are multiplicatively related to the optimized parameters. In order to reduce the use of computer resources and also in order to avoid the parameter results being missed, the design parameters need to be subjected to the analysis. In this paper, the sensitivity coefficient *CoP* is used to analyze the degree to which the four optimization objectives are affected by the variable parameters, and its value is calculated by the formula:

$$\begin{aligned} CoP(x_i) &= \left(1 - \frac{SS_E^P}{SS_r}\right) * (S_T^{MOP}(x_i)) \\ &= \left(1 - \frac{SS_E^P}{SS_r}\right) * \left(1 - \frac{V(f(x_i)\,|x_{\sim i})}{V(f(x_i))}\right) \end{aligned} \tag{12}$$

where SS_r is the amount of total variance, SS_E^p the amount of unexplained variance, $S_T^{MOP}(x_i)$ the total effect sensitivity factor, $V(f(x_i)x_{\sim i}$ the amount of variance of x_i triggered by the rest of the design parameters of $f(x_i)$, and $V(f\,(x_i))$ is the variance value of $f(x_i)$ generated by variables other than x_i. Using the OptiSlang module in the workbench, the specific values of the sensitivity of the design parameters to the objective function are calculated. Fig. 11 shows the calculation results of the software.

From the above analysis, different sizes of the magnetic bridge have different effects on the performance of the motor output. Meanwhile, the main objective of this paper is to improve the high-speed expansion capability of the motor by improving the magnetization capability of the motor. Therefore, the four optimization objectives are given different weights. Its expression is shown in Eq. (13):

$$\begin{aligned} S(x_i) \;=\; & \lambda_{\delta d}CoP_{\delta d}(x_i) + \lambda_{\delta u}CoP_{\delta u}(x_i) \\ & + \lambda_{Bd}CoP_{Bd}(x_i) + \lambda_T CoP_T(x_i) \end{aligned} \tag{13}$$

TABLE 2. *CoP* of prognosis and comprehensive trend-off index.

Design variables	Optimization objectives				index
	δ_u	δ_d	B_d	T	
alpha	−9.74	16.8	6.88	9.36	10.886
l_{pm}	11.87	−9.63	−13.82	20.66	14.42
w_o	9.45	6.48	4.92	−13.06	8.283
w_i	2.79	−6.35	5.93	−19.38	9.777
w_{co}	−15.75	−1.54	4.78	6.27	5.352
w_{ci}	1.28	−3.39	0.99	3.99	2.639
l_{ou}	2.93	−3.28	1.02	−0.85	1.838
l_{od}	0.80	−3.28	1.61	−0.66	1.745
l_{iu}	9.37	3.84	6.77	0.55	4.285
l_{id}	1.1	−4.70	−3.59	0.31	2.69

where x_i is the design parameter, for the design variables to the four optimization objectives to give different weight allocations. $\lambda_{\delta d}$, $\lambda_{\delta u}$, λ_{Bd}, and λ_T are the optimization objectives of magnetization enhancement ratio, weak magnetism ratio, weak magnetism harmonics percentage, and output torque capacity percentage of the weight factor, respectively. In this paper, weak magnetic performance enhancement is the main focus, and the influence of motor tooth harmonics on output torque pulsation is also taken into account, with values of 0.1, 0.3, 0.3, and 0.3, respectively. Calculations based on Eq. (13) show that the distribution of the trade-off coefficients of each design structural parameter for the output optimization objective is shown in Table 2.

Based on the results of the distribution of the trade-off coefficients, the weakly sensitive coefficient parameters are maintained at the initial design value. The strongly sensitive layer parameters continue to participate in the genetic algorithm optimization. The trade-off coefficients of the motor structure variables are greater than 4 for the strong sensitive layer parameters and less than 4 for the weak sensitive layer parameters, and the stratification results are shown in Table 3. According to the result of sensitivity stratification, it can be seen that 6 variables are involved in the genetic algorithm, which not only minimizes the computer resources but also maximizes the optimal solution in global optimization.

TABLE 3. Design parameter sensitivity stratification.

Sensitive	alpha, l_{pm}, w_o, w_i, w_{co}, l_{iu}
Insensitive	w_{ci}, l_{ou}, l_{od}, l_{id}

3.4. Multi-Objective Optimization Results

According to the constraints on the objective function, the multi-objective optimization particle swarm results in comprehensive analysis to obtain the optimal solution of the design parameters. The position in the calculation of the particle swarm results is shown in Fig. 12.

After bringing the optimized dimensioning results into the software calculations, a comparison of the specific values of the variable parameters given for the six strongly sensitive layers

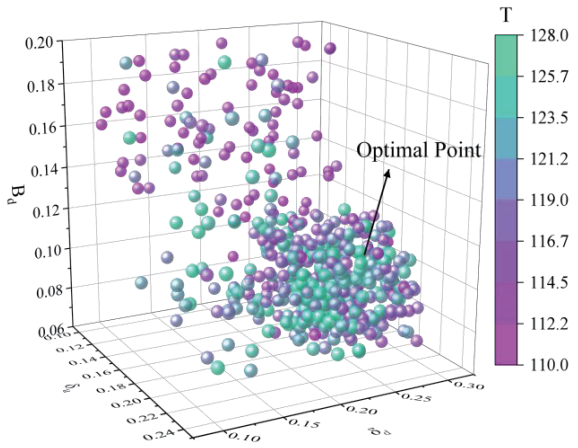

FIGURE 12. Particle swarm distribution.

and the four target variable parameters before and after optimization is obtained as shown in Table 4.

From the data in Table 4, it can be seen that after the multi-objective optimization, the change of its magnetic load in the demagnetized state of the motor compared with the unexcited state is increased from 0.2 to 0.266, and the magnetization ability is improved by 33%. The output torque of the motor is in-

TABLE 4. Comparison of structural parameters before and after optimization.

Design variables	Initial values	Optimal values
alpha	110 deg	124 deg
l_{pm}	16 mm	20.6 mm
w_o	2 mm	1.65 mm
w_i	2 mm	2.78 mm
w_{co}	9.65 mm	8.35 mm
l_{iu}	6 mm	7.31 mm
δ_u	0.45	0.196
δ_d	0.2	0.266
B_d	0.23	0.08
T	112 N·m	123 N·m

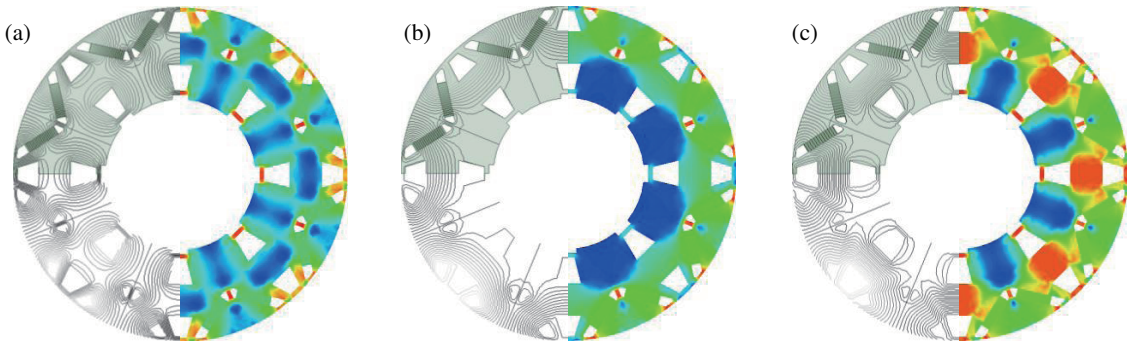

FIGURE 13. Motor magnetic field distribution before optimization. (a) Demagnetization. (b) Non-magnetic. (c) Magnetization.

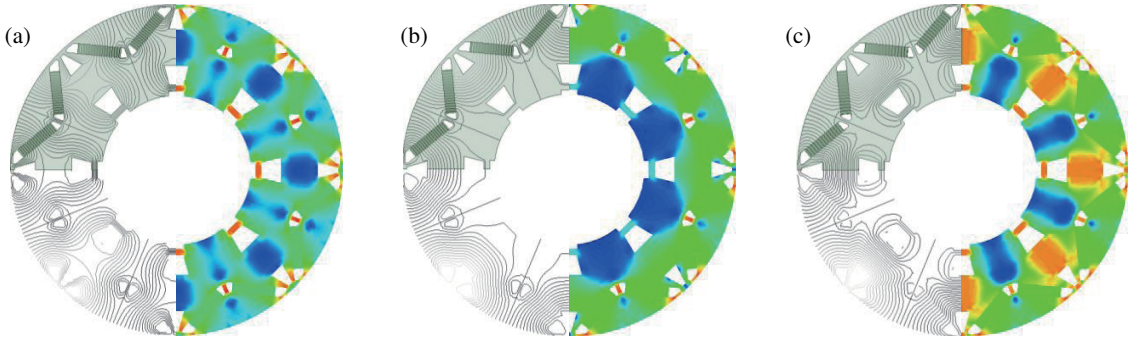

FIGURE 14. Motor magnetic field distribution after optimization. (a) Demagnetization. (b) Non-magnetic. (c) Magnetization.

creased from 112 to 123 N·m with an optimization amplitude of 9.8%. The amplitude of the 11th and 13th air-gap magnetism harmonics under the motor's unexcited magnetism is reduced from 0.23 to 0.08, and the harmonic ratio is weakened by 65.3%. In summary, the optimal solution selected after multi-objective optimization satisfies the objective function and constraints, and the performance of the motor is greatly improved.

4. ELECTROMAGNETIC ANALYSIS

Through the calculation of multi-objective optimization, the structural parameters of the motor are optimized, and the output performance of the motor is improved. In order to verify whether the weak magnetic speed expansion capacity of the motor is effectively increased after the optimization, it is necessary to carry out a comparative analysis through the calculation of the accurate electromagnetic field simulation of the motor before and after the optimization. The electromagnetic performance of the motor is comprehensively resolved by analyzing the parameters such as air gap magnetism, dq-axis inductance, and output torque of the motor before and after the optimization of the motor in the three states of magnetizing, demagnetizing, and no excitation.

4.1. No-Load Characteristics

The no-load magnetic field distributions before and after the optimization of the motor are shown in Figs. 13 and 14. From Fig. 13 and Fig. 14, it can be seen that the optimized motor has a wider rotor main magnetic circuit with better demagnetization effect and more uniform distribution of magnetic lines. Under unexcited state, the leakage of magnetism at the end of the permanent magnets is smaller after optimization. Under the magnetization enhancement state, the distribution of magnetic field strength of the magnetic bridge is more reasonable, and the saturated area of the motor is reduced, which proves the correctness of the results of the multi-objective optimization.

In order to compare the output performance of the motors in this paper, a rotor punch model of a conventional motor with the same power is designed in Fig. 15.

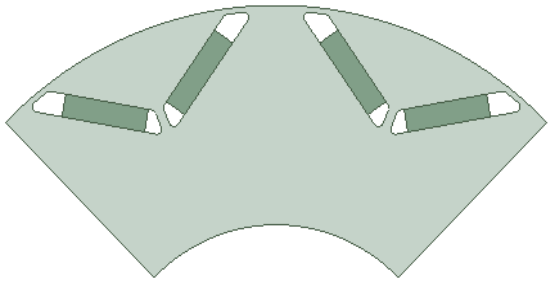

FIGURE 15. Conventional built-in motor rotor structure.

The output parameters such as the sinusoidal degree of the motor's reverse electromotive force and the motor's iron consumption are related to the harmonic content of the motor's air-gap magnetism. Fig. 16 shows the distributions of the motor's air-gap magnetism before and after the optimization and the harmonic components of the motor's air-gap magnetism. Af-

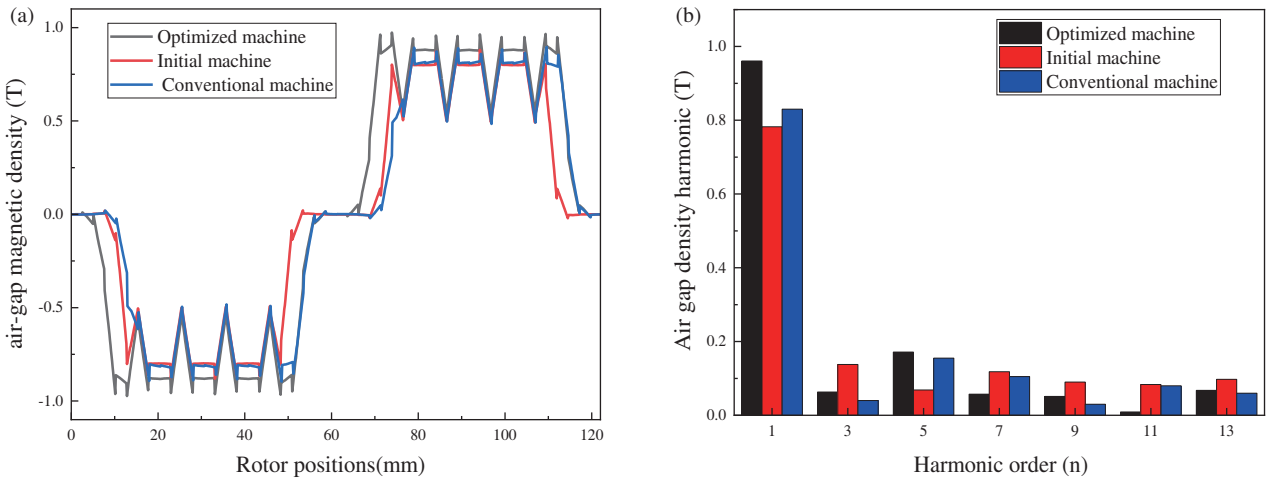

FIGURE 16. Air-gap flux density of optimized machine, initial machine and conventional PMSM. (a) Waveforms. (b) Harmonics.

ter optimization, the clamping angle of the motor permanent magnets increases, and the motor air-gap magnetism pole arc coefficient increases accordingly; the motor air-gap magnetism fundamental wave component increases, and the motor magnetic load increases correspondingly. The 3rd, 7th, 9th, 11th, and 13th harmonics are significantly diminished, while the fifth harmonic exhibits a notable increase in comparison to the pre-optimization period. The proportion of the 11th and 13th harmonics in the fundamental waveform is reduced from 23% to 8%. This reduction in harmonics is conducive to the weakening of the motor output torque pulsation, as it reduces the rate of air-gap magnetization distortion in the motor.

4.2. High-Speed Weak Magnetic Analysis

The analysis indicates that the motor's magnetic performance is significantly enhanced by the injection of a rotor demagnetizing current at high speed. In order to fit the high-speed external characteristic curve of the motor, the discrete scanning method is employed. The specific steps involved are as follows:

(1) The speed region is discretized when the motor is in the weak magnetic spreading speed I region. By scanning the maximum motor current value $I_{\max}$, different current angles *alpha* and different demagnetization current values I_{line} at different rotational speed points are used to calculate whether the terminal voltage of the motor reaches the limit value in various states. We calculate whether the terminal voltage of the motor reaches the limit value in various states and find the minimum *alpha* and I_{line} at this time to depict the output torque and output power of the motor. The corresponding mathematical expression is as follows:

The mathematical model of motor output voltage for different parameters of motor scanning is shown in Eq. (14):

$$U_n = F(alpha, I_{line}, n) \tag{14}$$

To find the minimum *alpha* when the terminal voltage reaches the maximum voltage, I_{line} mathematical model is shown in Eq. (15):

$$\begin{aligned} &\frac{\partial(F(alpha, I_{line}, n))}{\partial(alpha)} = 0, \ \frac{\partial(F(alpha, I_{line}, n))}{\partial(I_{line})} = 0 \\ &U_n = U_{\max}, \quad I_{line} = \min(I_{line}) \\ &alpha = \min(alpha) \\ &P = P(\min(alpha), \quad \min(I_{line}), n) \\ &T = T(\min(alpha), \quad \min(I_{line}), n) \end{aligned} \tag{15}$$

U_n in the above equation is the value of the motor terminal voltage at different speeds.

(2) The speed region is discretized when the motor is in the weak magnetic spreading speed II region. By scanning the motor armature current value I under different current angles *alpha* at different rotational speed points, we calculate whether the terminal voltage of the motor in various states reaches the limit value and find the maximum I and minimum *alpha* at this time, depicting the output torque and output power of the motor with the mathematical expression:

The mathematical model of motor output voltage for different parameters of motor scanning is shown in Eq. (16):

$$U_n = F(I, alpha, n) \tag{16}$$

To find the minimum *alpha* when the terminal voltage reaches the maximum voltage, I_{line}, a mathematical model is shown in Eq. (17):

$$\begin{aligned} &\frac{\partial(F(I, alpha, n))}{\partial(alpha)} = 0, \quad \frac{\partial(F(I, alpha, n))}{\partial(I)} = 0 \\ &U_n = U_{\max}, \quad I = \max(I) \\ &alpha = \min(alpha) \\ &P = P(\max(I), \quad \min(alpha), n) \\ &T = T(\max(I), \quad \min(alpha), n) \end{aligned} \tag{17}$$

From the above two steps, the weak magnetic speed expansion external characteristic curve of the motor in this paper can

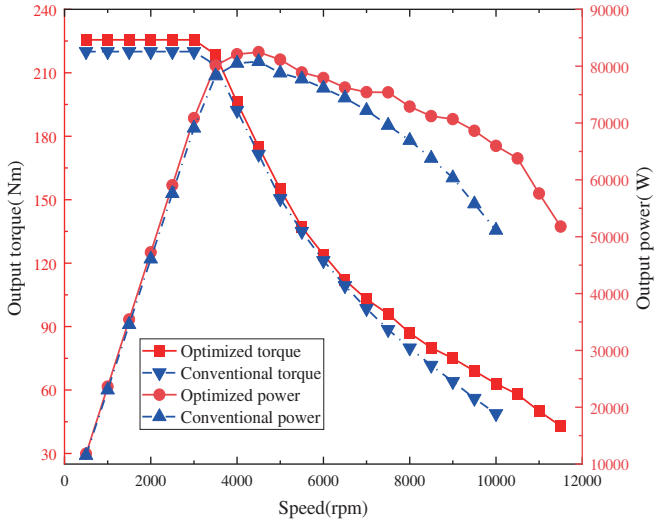

FIGURE 17. Distribution of motor external characteristic curves.

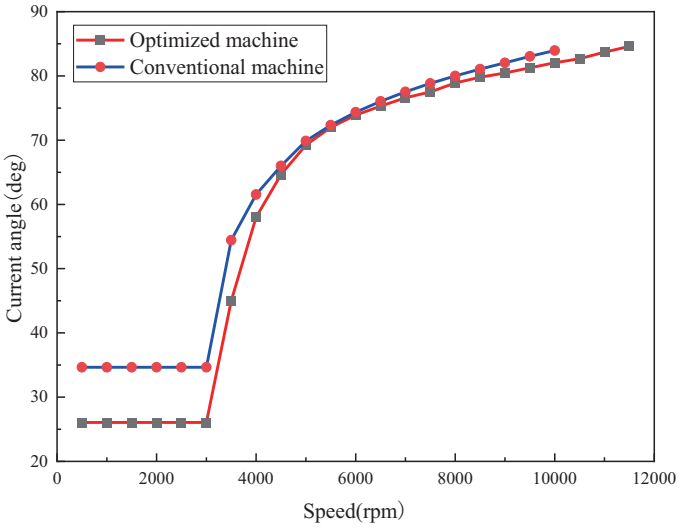

FIGURE 18. Distribution of current angle with increasing rotational speed.

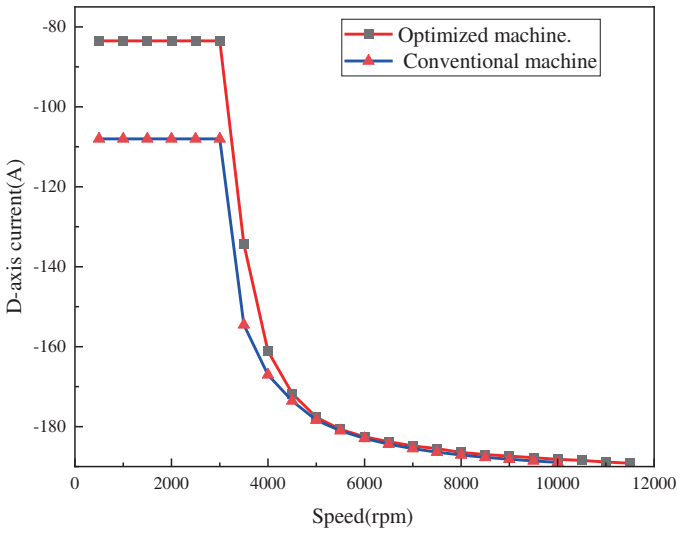

FIGURE 19. Distribution of d-axis current with increasing speed.

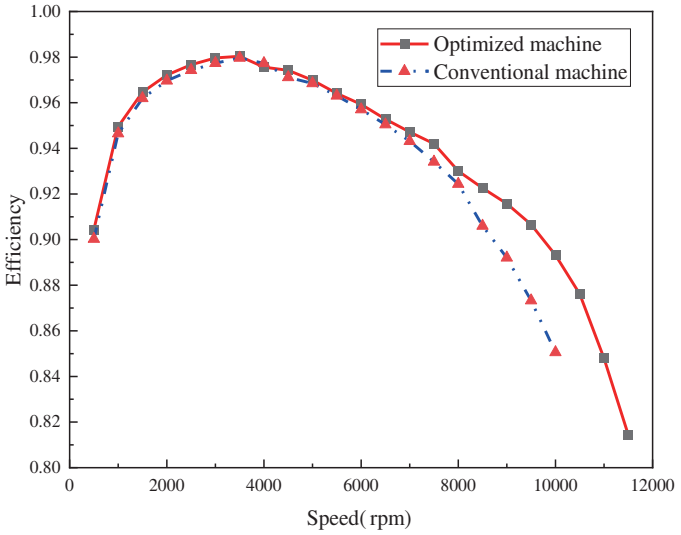

FIGURE 20. Distribution of motor efficiency with increasing rotational speed.

be obtained through finite element analysis calculation. The optimized motor model and conventional motor external characteristic curve are shown in Fig. 17. As can be seen from the figure, below the rated speed, the magnetic load of the optimized motor is higher than that of the conventional motor, so its output torque is higher. In comparison to the conventional built-in permanent magnet synchronous motor, the optimized motor exhibits a notable enhancement in its maximum speed, rising from 10,000 rpm to 11,500 rpm, which represents a 15% improvement in the motor's speed expansion capability. Furthermore, the output torque is augmented during high-speed operation, thereby ensuring that the output power of the motor is consistently superior to that of the traditional motor during the weak magnetic speed expansion. The power of conventional motors decreases rapidly after reaching maximum output power, and the power of optimized motors decreases slowly after reaching maximum output power, i.e., optimized motors have a wider power range. The optimized motor changes the current distribution ratio of the motor at high speed due to the high-speed injection of rotor demagnetizing current. The distribution of the current angle and d-axis current with an increase in speed is plotted in Fig. 18 and Fig. 19.

In this paper, the motor is slotted at the rotor q-axis position, and the inductive convexity and reluctance torque of the motor are reduced. As can be seen from Fig. 18, the current angle of the optimized motor with maximum torque at base speed is 26 deg, while that of the conventional motor is 34 deg. It has been demonstrated that the angle of the optimized motor is consistently less than that of the conventional motor when it operates at high speeds. Furthermore, it has been shown that the rotor demagnetization current can effectively alter the current distribution of the motor at high speeds. From Fig. 19 it can be seen

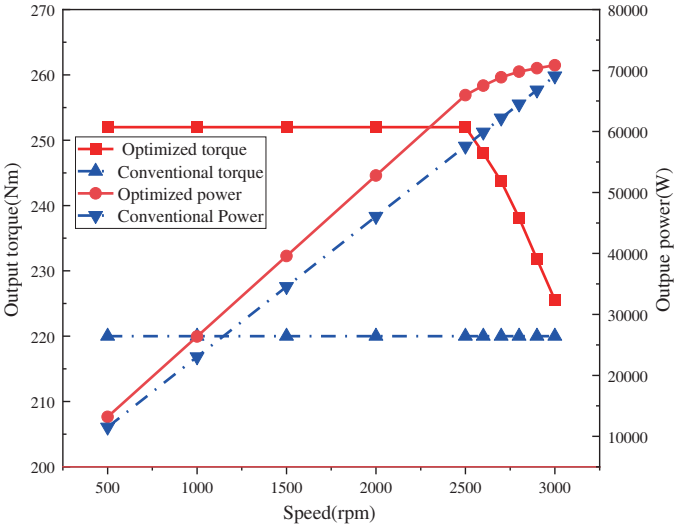

FIGURE 21. Motor output performance distribution with speed.

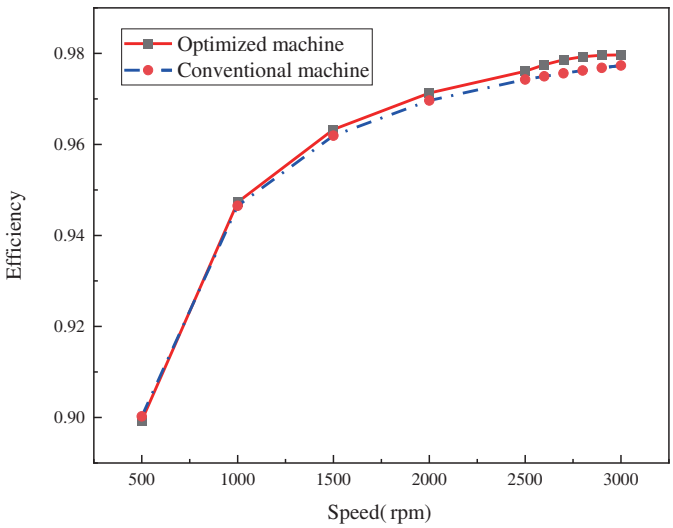

FIGURE 22. Power-speed curves of the two machines speed domain range.

that the d-axis current of the optimized motor is always smaller than that of the conventional motor when it is running at high rotational speed through the auxiliary demagnetizing effect of the rotor demagnetizing current. The motor requires high output power and should also have high efficiency. Fig. 20 shows the distribution of two kinds of motor efficiency with the increase of rotational speed. The efficiency of the optimized motor in this paper is higher than that of the conventional motor in the speed range. The efficiency distributions of the two motors are basically the same when the speed is 500 rpm-8000 rpm. The efficiency of the optimized motor decreases slowly and is significantly higher than that of the conventional motor when the speed is greater than 8000 rpm.

A comparative analysis was conducted to evaluate the output torque, output power, current distribution, and efficiency of the motor at varying speeds between the optimized motor and conventional motor. It can be demonstrated that the output performance of the optimized series hybrid excitation permanent magnet synchronous motor with weak magnetic speed expansion is markedly enhanced.

4.3. Low-Speed High Torque Analysis

The motor at low speed usually corresponds to the starting state of the car, and at this time the larger the starting torque is, the better the acceleration ability of the motor is. So this subsection calculates the output performance of the motor in this paper in the low-speed case.

According to the analysis, it can be seen that the magnetic load performance of the motor is greatly improved by injecting the rotor magnetizing current at low speed. The discrete scanning method is used to fit the low-speed external characteristic curve of the motor. The steps are: Keeping the current value and current angle of the motor armature unchanged, the rotor magnetizing current is set to the maximum value, at which time the motor speed value is scanned. When the output voltage of the motor is the maximum voltage, the motor speed continues to increase accompanied by a decrease in magnetizing current until the motor reaches the rated speed state. The external characteristic curve of the motor at low speed is shown in Fig. 21, which shows that when the rotor magnetizing current is 20 A, the maximum speed of the motor is 2500 rpm; the optimized motor output torque is 252 N·m; the output torque of the traditional motor is 220 N·m; and the starting torque of the motor was improved by 14.5%. As the motor speed increases from 2500 to 3000 rpm, the rotor magnetizing current declines to 0. Concurrently, the output torque diminishes from 252 N·m to 225 N·m. Notably, the output torque and output power of the motor in this study exceed those of the conventional motor in the low-speed range. Fig. 22 shows the efficiency distribution of the motor at low speed. Although the magnetizing current will bring additional stator copper loss, the higher output power of this paper's motor makes its low-speed efficiency higher than that of the traditional motor.

A comparison of the output torque, output power, and efficiency of the motor with the rotational speed of the two motors was conducted. This paper demonstrates that the output performance of the optimized series hybrid excitation permanent magnet synchronous motor with low speed and high torque has been significantly enhanced.

5. CONCLUSION

In this paper, a new series-connected hybrid excitation permanent magnet synchronous motor topology is proposed. It solves the engineering problems of poor high-speed speed expansion capability and small low-speed torque output of the traditional built-in permanent magnet synchronous motor. The magnetic field distribution and magnetic load distribution before and after optimization are calculated comparatively, and the rotor structure parameters of the motor are dynamically optimized. The no-load characteristics of the optimized motor and a conventional motor of the same power are examined separately, and the output performance is found to exceed that of

the conventional motor. A comparison and analysis of the output torque, output power, efficiency, and current distribution parameters of the two motors in the full-speed domain is conducted using the speed discretization method. The results show that the proposed series hybrid excitation permanent magnet synchronous motor achieves the desired effect of improving the output torque of the motor at low speeds and increasing the speed expansion capability at high speeds by the structural features and control methods of injecting the excitation current in the rotor.

REFERENCES

[1] Liu, Z., J. He, and C. Zeng, "Recent progress and future prospects of grain boundary diffusion technology for high-performance NdFeB permanent magnets," *Magnetic Materials and Devices*, Vol. 54, No. 04, 97–106, 2023.

[2] Liu, Z. and J. He, "Several issues on the development of grain boundary diffusion process for Nd-Fe-B permanent magnets," *Acta Metall Sin*, Vol. 57, No. 9, 1155–1170, 2021.

[3] Amara, Y., S. Hlioui, H. B. Ahmed, and M. Gabsi, "Power capability of hybrid excited synchronous motors in variable speed drives applications," *IEEE Transactions on Magnetics*, Vol. 55, No. 8, 1–12, Aug. 2019.

[4] Ai, Q., H. Wei, T. Li, L. Fan, and Y. Zhang, "Optimisation of reverse salient rotor for interior permanent magnet synchronous motor and experimental validation," *IET Electric Power Applications*, Vol. 15, No. 12, 1547–1563, 2021.

[5] Gao, M., Z. Yu, W. Jiao, W. Hu, H. Geng, Y. Liu, S. Liu, and Y. Liu, "Study on electromagnetic performance of permanent magnet rotor and dual stator starter generator for electric vehicle range extender," *Progress In Electromagnetics Research B*, Vol. 106, 39–55, 2024.

[6] Wu, Y., X. Xiong, and R. Ge, "Optimization study on high power density of high power naturally cooled motor based on NS-GA-III algorithm," *Digital Manufacturing Science*, Vol. 21, No. 4, 272–275, 2023.

[7] Lin, Q., Z. Huang, and Z. You, "Optimization analysis of high torque density industrial rare earth permanent magnet synchronous motor based on electromagnetic and temperature field coupling," *Fujian Metallurgy*, Vol. 52, No. 05, 61–63, 2023.

[8] Wang, W., S. Wang, and Y. Zhang, "Research on weak magnetic control strategy of built-in permanent magnet synchronous motor," *Journal of Northwestern Polytechnical University*, Vol. 36, No. 05, 970–977, 2018.

[9] Gao, G., R. Qu, and H. Shi, "A review of control strategies for the full-domain high-efficiency operation of wide-speed permanent magnet synchronous motors," *Chinese Journal of Electrical Engineering*, Vol. 43, No. 07, 2496–2512, 2023.

[10] Wang, J., H. Yu, and X. Meng, "Voltage closed-loop adaptive weak magnetism control of asynchronous motor considering reverse electromotive force," *Journal of Electrical Engineering*, 1–8, 2023.

[11] Xu, P., "Identification method of permanent magnet synchronous motor rotational error angle based on *d*-axis current error," *Electrical Drives*, Vol. 51, No. 20, 56–59, 2021.

[12] Zhang, J., K. Wang, and L. Gu, "Singlephase outofphase compromise fault-tolerant control of dual three-phase permanent magnet motor based on minimum copper consumption and maximum torque," *Flight Control and Detection*, Vol. 5, No. 01, 67–74, 2022.

[13] Xu, L. and T. Dong, "Application of improved overmodulation strategy in wide speed range control of automotive IPMSM," *Electrotechnology*, No. 21, 20–22, 2022.

[14] Zhao, H., "Topology optimization of synchronous reluctance machines," *Henan Science and Technology*, Vol. 42, No. 20, 12–16, 2023.

[15] Lu, R., Z. Liu, X. Liu, J. Liang, W. Wu, and W. Wang, "Electromagnetic characteristic analysis and optimization of a novel reverse salient PMSM for wide speed range," *Progress In Electromagnetics Research C*, Vol. 140, 105–115, 2024.

[16] Qiu, H., X. Ma, and B. Xiong, "Working principle and characteristic study of magnetic moment double-regulating axial radial hybrid excitation motor," *Journal of Electrical Machines and Control*, 1–17, 2023.

[17] Zou, Y., X. Liu, and T. Sun, "Design and electromagnetic characterization of a novel mechanical variable drainage permanent magnet motor," *Electric Drive*, Vol. 52, No. 4, 2022.

[18] Tessarolo, A., M. Mezzarobba, and R. Menis, "Modeling, analysis, and testing of a novel spoke-type interior permanent magnet motor with improved flux weakening capability," *IEEE Transactions on Magnetics*, Vol. 51, No. 4, 1–10, Apr. 2015.

[19] Tessarolo, A., M. Mezzarobba, and R. Menis, "A new rotor design for flux weakening capability improvement in spoke-type interior permanent magnet synchronous machines," in *2014 Ninth International Conference on Ecological Vehicles and Renewable Energies (EVER)*, 1–9, Monte-Carlo, Monaco, 2014.

[20] Cinti, L., C. Contò, and N. Bianchi, "A comparison between hybrid excited permanent magnet and wound rotor motor," in *2022 International Symposium on Power Electronics, Electrical Drives, Automation and Motion (SPEEDAM)*, 14–19, Sorrento, Italy, 2022.

[21] Feng, W. and K. Guo, "Optimized design of rotor structure for low-torque pulsating permanent magnet-assisted synchronous reluctance motor," *Electric Machines and Control Application*, Vol. 51, No. 9, Sep. 2024.